I. Shtablavyi, N. Popilovskyi, Yu. Nykyruy, and S. Mudry

Selective laser sintering of amorphous nanoparticles: Molecular dynamics simulations

Department of Metal Physics, Ivan Franko National University of Lviv, Lviv, Ukraine, ihor.shtablavyi@lnu.edu.ua

The paper investigates the process of liquid-phase sintering of amorphous iron-based nanoparticles by the method of molecular dynamics simulations. The classical molecular dynamics package LAMMPS was used for modeling. Visual analysis of the atomic configurations of nanoparticles during their rapid cooling revealed the self-purification effect of the particles. Partial pair correlation functions and coordination number distribution functions were used to analyze the atomic structure of nanoparticles after sintering. As a result of the analysis of the main structural parameters, which were obtained using the specified functions, differences in the atomic composition and structure of the volume and surface of nanoparticles were established.

Keywords: Selective laser melting, nanoparticles, liquid phase sintering, molecular dynamics method, pair correlation functions, coordination number distribution functions.

Introduction

New technological and engineering solutions require materials with a unique combination of mechanical, electrical, and magnetic properties. As is known, the properties of materials depend not only on the atomic composition, but also on the phase composition and atomic structure. Using different methods of synthesis of materials with the same atomic composition, it is possible to obtain a final product with different physical properties. Classical methods of obtaining polycrystalline materials use the dependence of the grain size on the speed of crystallization and heat treatment in the crystalline state [1, 2]. Taking this into account, it is possible to obtain a fine-crystalline material characterized by high strength and plasticity [3-8]. However, the polycrystalline structure of materials is coupled with the presence of grain boundaries, which can negatively affect the properties due to the inhibition of the movement of dislocations, intercrystalline corrosion, etc. Unlike polycrystalline materials, defect-free single crystals have much better properties, but obtaining them with given dimensions and configuration is a complex technological process. Another negative feature of single crystals is the anisotropy of properties, which is undesirable for many engineering solutions.

In contrast to mono- and polycrystalline materials, amorphous metal alloys are characterized by the absence of grain structure and, accordingly, grain boundaries, and amorphous alloys are isotropic in their properties. Considering this, their physical properties significantly exceed the properties of traditional metal alloys [9-11], so such materials can replace traditional ones in the technologies of the future. However, the main disadvantage of amorphous materials is the need to ensure high cooling rates during their production, which is possible only if their geometric dimensions are limited [12-14]. Despite the intensive search for alloys that require a lower cooling rate for amorphization, currently the diameter of bulk amorphous alloys is in the range of 30-80 mm [15-17]. Therefore, it was proposed to use thermoplastic molding methods [18] for the production of volumetric products from amorphous alloys, although these methods do not allow the production of products of any configuration and size. With this in mind, it is necessary to develop other technologies for obtaining volumetric products based on amorphous alloys.

In recent years, additive manufacturing technologies

have become increasingly widespread [19-21], which is due to the possibility of rapid production of products of almost any configuration using one device (3D printer). In contrast to 3D printing technologies with polymer materials, printing metal products is not so affordable. The reason for this is the significant activity of molten metals in relation to air oxygen, as well as in many cases unsatisfactory mechanical properties of materials immediately after 3D printing. Mainly, the mechanical properties deteriorate due to the polycrystalline nature of the materials and defects in the connection of the particles in the case of their laser sintering. The solution to this problem can be the use of amorphous metal alloys for 3D printing [22, 23]. The formation of amorphous materials using additive technologies allows avoiding polycrystalline structure, and also makes it possible to form volumetric amorphous alloys of such sizes and shapes that cannot be obtained by traditional methods.

However, the main problem in the formation of amorphous materials by this method is their crystallization after laser melting. Crystallization can be avoided by quickly removing heat from the sintering particles, as well as by choosing optimal thermodynamic sintering conditions. The study of this problem by experimental methods is not always possible due to the significant speed of phase transformations. Therefore, computer modeling methods can be used to study the sintering processes of amorphous particles at the atomic level and thus optimize the experimental conditions by obtaining preliminary results regarding the 3D printing process.

One of the most effective methods of modeling the structure and properties of materials is the molecular dynamics (MD) method. This method has been repeatedly used to model the structure and properties of both bulk and nanoscale materials. The MD method was also used to model the sintering process of single-component [24-27] and two-component crystalline nanoparticles [28, 29]. Unfortunately, we did not manage to find works where modeling of the sintering process of amorphous nanoparticles was carried out. In work [24] it was established that the process of sintering of nanoparticles can be divided into three stages. At the first stage, the rapid formation of a connecting neck between particles takes place mainly due to intensive surface diffusion of atoms. The second stage corresponds to the stable growth of the neck, which in the third stage grows rapidly. The mechanical properties by the MD method were studied in [28], and the sintering kinetics of aluminum nanoparticles was studied in [26], where it was shown that the time required for the coalescence of two particles is 30 ps. In [27], a large-scale simulation of the process of laser sintering of an array of iron nanoparticles placed on a substrate was carried out.

In this work, the process of sintering of amorphous iron-based nanoparticles and the conditions of their further amorphization after cooling were studied by the method of molecular dynamic modeling. Research was carried out at different temperatures. Results were obtained that can be used to optimize the process of 3D printing of amorphous materials by experimental methods.

I. Methodology of modeling

The study of the sintering process of nanoparticles was carried out by the method of molecular dynamics using the free open package for classical molecular dynamics LAMMPS [30]. OVITO tools [31] were used to visualize the obtained results, which allow not only visualization of the modeling process, but also some calculations. To calculate the interatomic interaction forces, the modifiedembedded atom potential (MEAM) [32, 33] was used, which is often used to model systems based on Al, Si, Mg, Cu, and Fe. The initial velocities of atoms for each of the studied temperatures were calculated according to the Maxwell-Boltzmann distribution. Integration of the equations of motion was carried out with a timestep of 2 fs. Simulations were performed in an isothermal-isochoric ensemble (NVT) using an orthogonal simulation cell. The density of the alloys was set according to the experimental values. Constant temperature was maintained using a Nose-Hoover thermostat and a barostat with a temperature damping parameter of 0.1 ps. The spatial configuration of atoms was recorded, as a rule, at every hundredth subsequent time step. The simulation duration was equal to $5 \cdot 10^5$ time steps.

The modeling consisted of two stages. At the first stage, cubic cells with $Fe_{77}Cu_3Si_{20}$, $Fe_{78}Cu_2Si_{20}$ and $Fe_{79}Cu_1Si_{20}$ atoms were created, with a structure corresponding to amorphous alloys of this composition. For this, the specified alloys were heated to a temperature above the melting point and then quickly cooled. In this case, periodic boundary conditions were used. Spherical particles of the required diameter were cut from the obtained atomic configurations, from which complexes of two and three particles were formed (Fig. 1) for modeling the sintering process at the second stage of research. In this case, the cell size was much larger than the particle diameter and periodic boundary conditions were not used.

The simulation of the sintering process was carried out at temperatures in the range of 300–1800 K with a step of 100 K. Changes in partial interatomic distances and coordination numbers were studied for atomic configurations at different temperatures.

II. Results and discussion

The simulation of the sintering process was carried out for amorphous particles with the atomic composition of $Fe_{77}Cu_3Si_{20}$, $Fe_{78}Cu_2Si_{20}$ and $Fe_{79}Cu_1Si_{20}$ with a size of four nanometers. The sintering process was started at a temperature of 1811 K, that is, at a temperature above the melting point of iron, after which the temperature was lowered to room temperature at a rate of 10 K/s in order to reproduce the sintering modes in conditions close to real ones. The analysis of atomic configurations and displacements of atoms (Fig. 2 a, b) shows that the process of combining particles takes place already at the beginning of the simulation, and during the first seven picoseconds of the simulation, a neck is formed between two particles. During the next 700 picoseconds, the two particles merge, which is accompanied by a decrease in the surface energy [34] and transition to the equilibrium state of the particle at the given temperature. Similar processes occur with
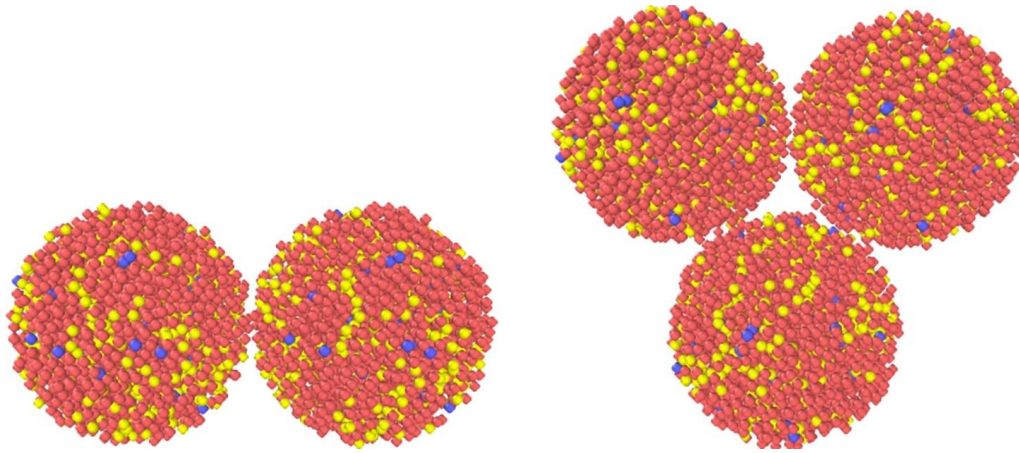
Fig. 1. Initial configurations of atoms in the simulation cells.

a)

b)

c)

d)
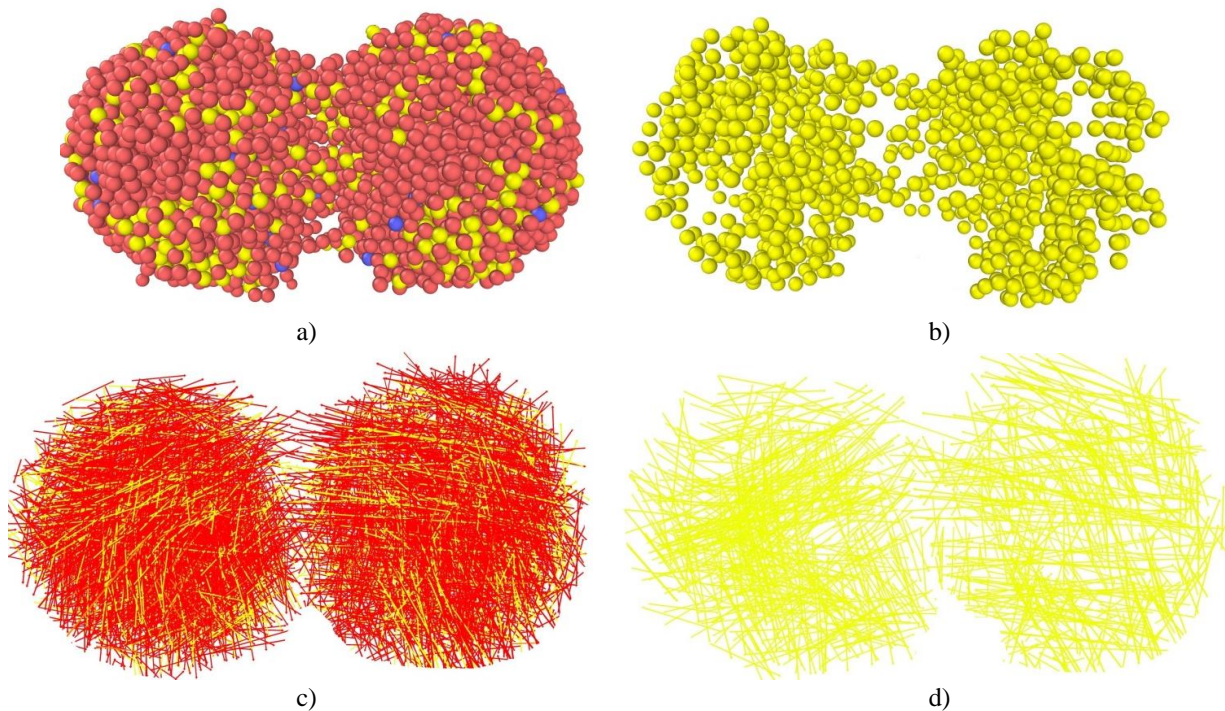
Fig. 2. Visualization of the process of liquid-phase sintering of two $Fe_{77}Cu_3Si_{20}$ nanoparticles at a temperature of 1811K (a – atomic configurations for all atoms and b – for silicon, c, and d corresponding images of atomic movements).

particles with the atomic composition $Fe_{78}Cu_2Si_{20}$ and $Fe_{79}Cu_1Si_{20}$.

The process of particle sintering can be described within the framework of the viscous flow model [35], according to which it can be divided into four stages. At the first stage, contact between particles occurs due to the movement of atoms, as a result of which the formation of a connecting neck begins. The second stage can be called the stage of preliminary neck growth between particles and it can last for 10-20 ps depending on the material of the particles and the sintering temperature. At the third stage, the final formation of the neck takes place (it can last 20-80 ps). During the fourth stage, the diffusion mixing of the particles is completed and they are finally merged.

Qualitative information about the mechanism of particle sintering can be obtained from the analysis of the displacement vectors of atoms of various types (Fig. 2 c, d). For such an analysis, within the particle volume, a set

of vectors is built, each of which belongs to a certain particle, the beginning of the vector corresponds to the position of the atom in the previous modeling step, and the end to the next one. Accordingly, the arrow indicates the direction of movement, and the length of the vector corresponds to the amount of movement of the atom. Figure 2 (c) shows the distribution of displacement vectors of all atoms for nanoparticles with the atomic composition $Fe_{77}Cu_3Si_{20}$ at a temperature of 1811 K, and Figure 2 (d) shows the displacement vectors for silicon atoms only. As we can see, surface atoms move mainly along the surface of particles, and between particles, the movement of atoms that belong to each of the particles has a direction from one particle to another. In addition, silicon atoms are displaced to greater distances compared to iron atoms. Copper atoms, which are small in number, almost do not participate in the diffusional mixing of particles, but move within the volume of each particle until they are completely united. For particles with the atomic

composition $Fe_{79}Cu_1Si_{20}$, where the copper content is lower, the movement of silicon atoms in the vicinity of the neck of the connection between the particles is the largest compared to other nanoparticles.

The analysis of atomic configurations by the visualization method allows only a qualitative description of the atomic structure of nanoparticles during sintering. For the quantitative analysis of the structure, total and partial pair correlation functions (PCFs) are used, which make it possible to interpret the topological and chemical short-range order arrangement of atoms. According to the simplest interpretation [36], the pair correlation function is the density of the probability of placing atoms at a certain distance from some atom located at the origin of the coordinate system. For crystalline materials with an ideal structure, which are characterized by a long-range arrangement of atoms, this function has the form of narrow maxima, the positions of which correspond to the

distances between atoms that are in different coordination spheres. For disordered systems, pair correlation functions have the form of continuous functions, the positions of maxima of which indicate the most probable distances between atoms.

The pair correlation functions calculated for the investigated nanoparticles at all temperatures do not show signs of the presence of traces of long-range order. As an example, Figure 4 shows partial PCFs for nanoparticles with the atomic composition of $Fe_{77}Cu_3Si_{20}$. Analogous functions obtained by us for a different content of atoms in nanoparticles have a similar appearance, therefore, it can be stated that at room temperature the studied particles are amorphous. It should also be noted that the height of the PCF maxima in this figure is overestimated due to the larger volume of the model cell compared to the size of the nanoparticles.

An unexpected feature of the partial pair correlation

a)   b)
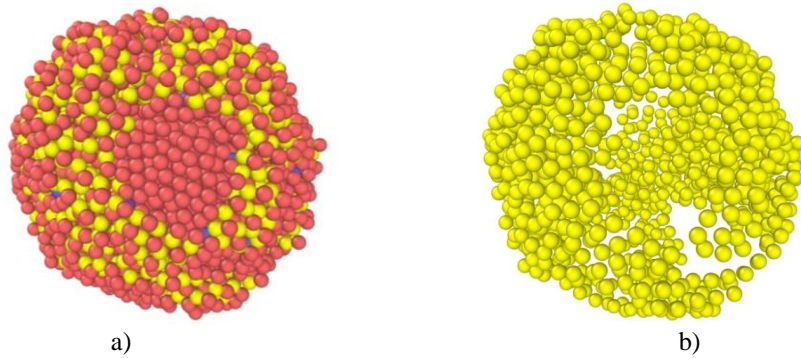
Fig. 3. Configuration of atoms in particles with the atomic composition $Fe_{79}Cu_1Si_{20}$ at a temperature of 300K (a – atomic configurations for all atoms and b – for silicon atoms).

a)   b)

c)   d)
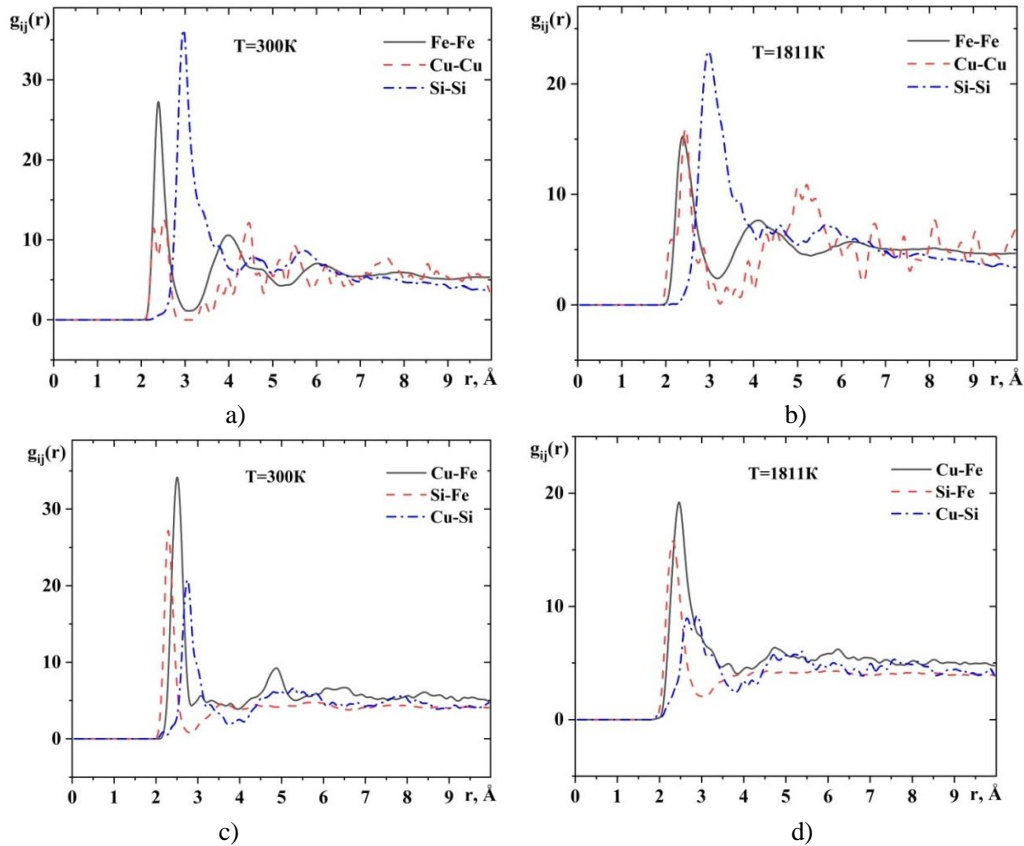
Fig. 4. Partial pair correlation functions for $Fe_{77}Cu_3Si_{20}$ nanoparticles at temperatures of 300K and 1811K.
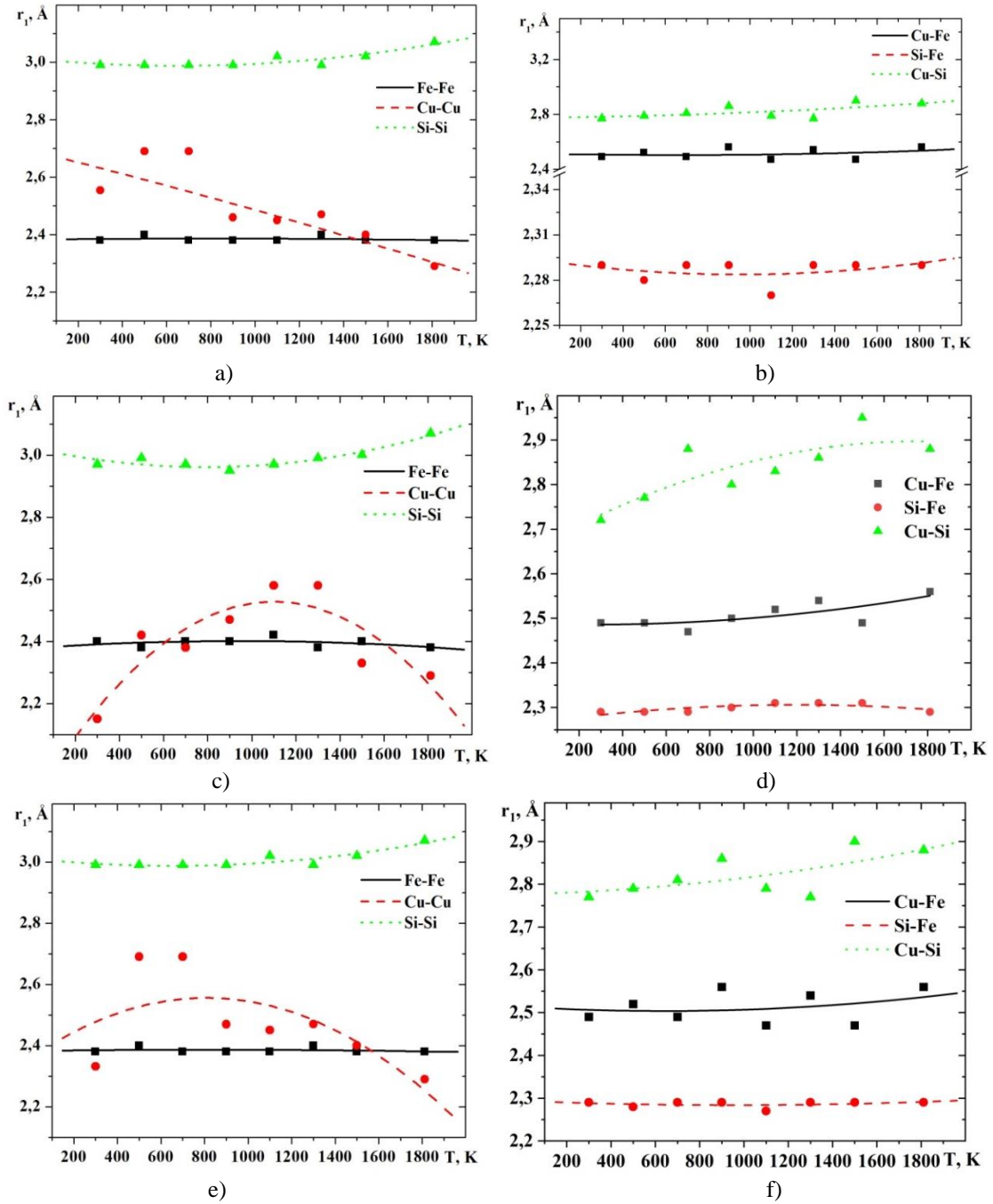
Fig. 5. The most probable partial interatomic distances depending on temperature for nanoparticles with the atomic composition $Fe_{77}Cu_3Si_{20}$ (a, b), $Fe_{78}Cu_2Si_{20}$ (c, d) and $Fe_{79}Cu_1Si_{20}$ (e, f).

functions for silicon is a significant shift in the position of the first maximum towards larger distances compared to pure silicon. Such a displacement is possible in the case of the formation of a solution of silicon and iron, as a result of which silicon is mainly surrounded by iron atoms, which increases the distance between the silicon atoms.

In order to analyze the temperature dependence of the most probable interatomic distances for the studied particles, the corresponding dependences were constructed, which are shown in Figure 5.

The trend of changing the most probable interatomic distances for nanoparticles with different atomic composition is similar. In particular, the distances between pairs of atoms decrease with decreasing temperature, only the Cu-Cu interatomic distances change non-

monotonically. In our opinion, the increase in the interatomic distances between copper atoms upon cooling to a temperature of about 1000 K is due to their dissolution in iron, after which the separation of copper into clusters with their subsequent segregation is observed. In this case, the distances between them decrease again.

The analysis of the distances between silicon atoms deserves special attention. As we can see, immediately after sintering of nanoparticles, these distances are much larger than the distances between atoms in liquid and crystalline silicon (Table 1). As it follows from our assumptions, silicon is in solution with iron, as a result of which the first coordination sphere of silicon contains mainly iron atoms. This fact is confirmed by the small

distances between iron and silicon atoms (Fig. 5, b, d, e).

Detailed conclusions about the atomic distribution in nanoparticles can be made as a result of a generalized analysis of visualization of nanoparticles at the atomic level (Fig. 3), partial interatomic distances (Fig. 5) and partial coordination numbers (Figs. 6 and 7).

The profile of the partial coordination numbers distribution functions (Fig. 6) indicates the predominant neighborhood of Fe-Fe, Si-Si and partial Cu-Si atoms. It should also be noted that the nanoparticles after sintering contain a small number of structural units with a predominant neighborhood of iron and silicon atoms. Iron atoms, in turn, form two types of arrangement. One type with a coordination number close to eight, and the other with a coordination number of one or two, which is possible when forming a chain structure of iron. The indicated features are also reflected on the temperature dependences of the most probable values of the coordination numbers (Fig. 7). As we can see, all coordination numbers change slightly with temperature, only for silicon atoms there is a sharp decrease in the coordination number during rapid cooling of nanoparticles

from a temperature of about 1000 K. It should be noted that the indicated change in the coordination number of silicon can be explained on the basis of the predetermined segregation of silicon on the surface of nanoparticles. However, it should be clarified that as a result of the segregation of silicon, a small part of iron dissolves in it, which leads to an increase in interatomic distances and a decrease in partial Si-Si coordination numbers.

The described structural changes can be explained within the framework of the self-cleaning effect of nanoparticles. For the first time, this effect was observed in the case of doping semiconductor nanoparticles and was explained by an increase in the energy of solution formation with a decrease in the size of the particles [41-43]. An increase in the amount of alloying admixture and the volume of nanoparticles led to a decrease in this energy, which contributes to the formation of solutions.

As we can see from the results of our research, silicon and copper atoms are "pushed out" of the nanoparticle volume as a result of the self-cleaning effect, forming an atomic solution on the surface of the nanoparticle formed as a result of sintering. However, this phenomenon does

Table 1.

Atomic radii and coordination numbers of nanoparticle components

Chem. element	r (emp)[37], Å	r (calc)[38], Å	r (liq)[39], Å	Z (cr) [40]	Z (liq) [39]
Iron	1,4	1,51	1,24	12	10,6
Copper	1,35	1,45	1,285	12	11,3
Silicon	1,1	1,11	1,23	4	6,4

a)

b)

c)

d)
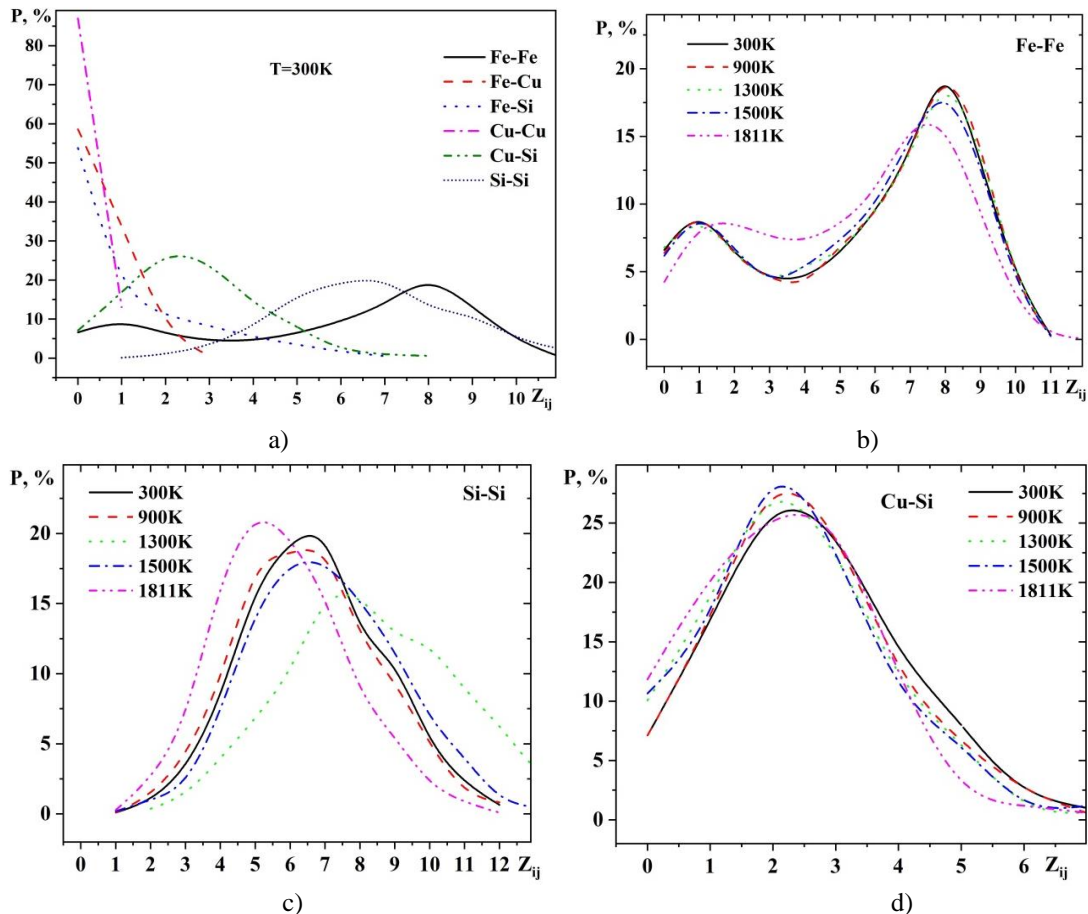
Fig. 6. Distribution of partial coordination numbers for $Fe_{77}Cu_3Si_{20}$ particles at different temperatures.
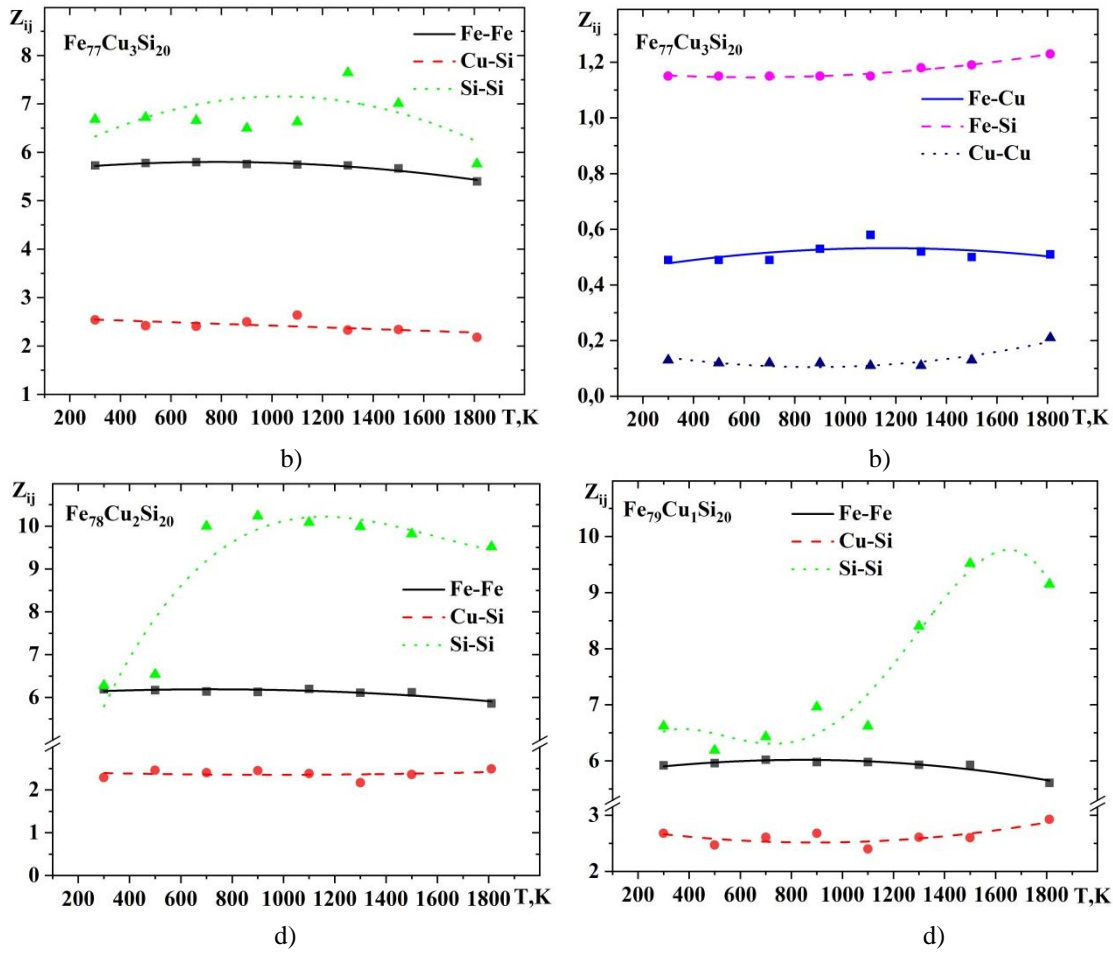
Fig. 7. Temperature dependence of partial coordination numbers for nanoparticles after sintering.

not lead to crystallization of nanoparticles during their rapid cooling.

Conclusions

In this work, the process of sintering of nanoparticles as a result of rapid heating and cooling was investigated by the method of molecular dynamics. It is shown that as a result of liquid-phase sintering of nanoparticles, the segregation of silicon and copper atoms occurs on the surface of nanoparticles and the formation of a surface solution of these atoms and iron. As a result, iron atoms tend to form two types of atomic arrangement. One type corresponds to a disordered iron structure with a coordination number of eight, and the other corresponds to a chain structure and is present in surface solution with silicon and copper.

The segregation of atoms on the surface of nanoparticles can be explained by the self-cleaning effect of nanoparticles, which is due to the dependence of the energy of solution formation on the size of the nanoparticle.

Shtablavyi I. – Doctor of Physical and Mathematical Sciences, Professor of Metal Physics Department, Ivan Franko National University of Lviv;
Popilovskyi N. – Ph.D. student of Metal Physics Department, Ivan Franko National University of Lviv;
Nykyruy Yu. – Ph.D., Associate Professor of Metal Physics Department, Ivan Franko National University of Lviv;
Mudry S. – Doctor of physical and mathematical Sciences, Professor, Head of Metal Physics Department Ivan Franko National University of Lviv.

[1] V. Anthony, Teran and Andreas Bill, *Time-evolution of grain size distributions in random nucleation and growthcrystallization processes*, Phys. Rev. B, 81(7), 075319 (2010); https://doi.org/10.1103/PhysRevB.81.075319.
[2] M. El Wahabi, L. Gavard, F. Montheillet, J.M. Cabrera, J.M. Prado, *Effect of initial grain size on dynamic recrystallization in high purity austenitic stainless steels*, Acta Materialia, 53(17), 4605 (2005); https://doi.org/10.1016/j.actamat.2005.06.020.

[3] J. Pelleg, Grain Size Effect on Mechanical Properties. In: Mechanical Properties of Silicon Based Compounds: Silicides (Engineering Materials, Springer, Cham, 2019); https://doi.org/10.1007/978-3-030-22598-8_13.

[4] R.B. Figueiredo, T.G. Langdon, *Effect of grain size on strength and strain rate sensitivity in metals*. J Mater Sci, 57, 5210 (2022); https://doi.org/10.1007/s10853-022-06919-0.

[5] M. Naghizadeh, H. Mirzadeh, *Effects of Grain Size on Mechanical Properties and Work-Hardening Behavior of AISI 304 Austenitic Stainless Steel,* Steel research international, 90(10), 1900153 (2019); https://doi.org/10.1002/srin.201900153.

[6] J. M. Maita, S. Rommel, J. R. Davis, H. Ryou, J. A. Wollmershauser, E. P. Gorzkowski, B. N. Feigelson, M. Aindow, S. Lee, *Grain size effect on the mechanical properties of nanocrystalline magnesium aluminate spinel*, Acta Materialia, 251, 118881 (2023); https://doi.org/10.1016/j.actamat.2023.118881.

[7] Y. Qin, P. Wen, D. Xia, H. Guo, M. Voshage, L. Jauer, Y. Zheng, J. H. Schleifenbaum, Y. Tian, *Effect of grain structure on the mechanical properties and in vitro corrosion behavior of additively manufactured pure Zn*, Additive Manufacturing, 33, 101134 (2020); https://doi.org/10.1016/j.addma.2020.101134.

[8] K. Zhou, B. Liu, Y. Yao, K. Zhong, *Effects of grain size and shape on mechanical properties of nanocrystalline copper investigated by molecular dynamics,* Materials Science and Engineering: A, 615, 92 (2014); https://doi.org/10.1016/j.msea.2014.07.066.

[9] L.-C. Zhang, Z. Jia, F. Lyu, S.-X. Liang, *A review of catalytic performance of metallic glasses in wastewater treatment: Recent progress and prospects*, Prog. Mater. Sci., 105, 100576 (2019); https://doi.org/10.1016/j.pmatsci.2019.100576.

[10] M. Jakab, J. Scully, *On-demand release of corrosion-inhibiting ions from amorphous Al–Co–Ce alloys*, Nature Mater, 4, 667 (2005); https://doi.org/10.1038/nmat1451.

[11] Y.C. Li, C. Zhang, W. Xing, S.F. Guo, L. Liu, *ACS Design of Fe-Based Bulk Metallic Glasses with Improved Wear Resistance*, Appl. Mater. Interfaces, 10, 43144 (2018); https://doi.org/10.1021/acsami.8b11561.

[12] A. L. Greer, Physical Metallurgy (Fifth Edition), Capter 4 - Metallic Glasses, (Elsevier, Amsterdam, 2014); https://doi.org/10.1016/B978-0-444-53770-6.00004-6.

[13] K. Russew, L. Stojanova, Most Important Methods for Production of Amorphous Metallic Alloys. In: Glassy Metals (Springer, Berlin, Heidelberg, 2016); https://doi.org/10.1007/978-3-662-47882-0_2.

[14] Si. Yamaura, W, Zhang, A, Inoue, Introduction to Amorphous Alloys and Metallic Glasses. Novel Structured Metallic and Inorganic Materials (Springer, Singapore, 2019); https://doi.org/10.1007/978-981-13-7611-5_1.

[15] Y. Yokoyama, E. Mund, A. Inoue, L. Schultz, *Production of $Zr_{55}Cu_{30}Ni_5Al_{10}$ Glassy Alloy Rod of 30 mm in Diameter by a Cap-Cast Technique*, Mater. Trans., 48, 3190 (2007); https://doi.org/10.2320/matertrans.MRP2007164.

[16] W.H. Wang, *Roles of minor additions in formation and properties of bulk metallic glasses*, Prog. Mater. Sci. 52, 540 (2007); https://doi.org/10.1016/j.pmatsci.2006.07.003.

[17] N. Nishiyama, K. Takenaka, H. Miura, N. Saidoh, Y. Zeng, A. Inoue, *The world's biggest glassy alloy ever made*, Intermetallics, 30, 19 (2012); https://doi.org/10.1016/j.intermet.2012.03.020.

[18] J. Schroers, *Processing of Bulk Metallic Glass*, Adv. Mater. 22, 1566 (2010); https://doi.org/10.1002/adma.200902776.

[19] O. Diegel, Comprehensive Materials Processing, 10.02 - Additive Manufacturing: An Overview, (Elsevier, Amsterdam, 2014); https://doi.org/10.1016/B978-0-08-096532-1.01000-1.

[20] E. Tempelman, H. Shercliff and B. Ninaber van Eyben, Manufacturing and Design Understanding the principles of how things are made (Elsevier, Amsterdam, 2014); https://doi.org/10.1016/C2011-0-08438-7.

[21] D. Godec, J. Gonzalez-Gutierrez, A. Nordin, E. Pei, J. Ureña Alcázar, A Guide to Additive Manufacturing (Springer, Cham, 2022); https://doi.org/10.1007/978-3-031-05863-9.

[22] Y. Shen, Y. Li, C. Chen, H. -L. Tsai, *3D printing of large, complex metallic glass structures*, Materials & Design, 117, 213 (2017); https://doi.org/10.1016/j.matdes.2016.12.087.

[23] C. Zhang, D. Ouyang, S. Pauly, L. Liu, *3D printing of bulk metallic glasses,* Materials Science and Engineering: R: Reports, 145, 100625 (2021); https://doi.org/10.1016/j.mser.2021.100625.

[24] Z. J. Liu, Q. Cheng, Y. Wang, Y. Li, J. Zhang, *Sintering neck growth mechanism of Fe nanoparticles: A molecular dynamics simulation*, Chemical Engineering Science, 218, 115583 (2020); https://doi.org/10.1016/j.ces.2020.115583.

[25] J. Guo, P. Ji, L. Jiang, G. Lin Y. Meng, *Femtosecond laser sintering Al nanoparticles: A multiscale investigation of combined molecular dynamics simulation and two-temperature model,* Powder Technology, 407, 117682 (2022); https://doi.org/10.1016/j.powtec.2022.117682.

[26] S. Kurian, R. Mirzaeifar, *Selective laser melting of aluminum nano-powder particles, a molecular dynamics study*, Additive Manufacturing, 35, 101272 (2020); https://doi.org/10.1016/j.addma.2020.101272.

[27] K. Peng, H. Huang, H. Xu, Y. Kong, L. Zhu, Z. Liu, *A molecular dynamics study of laser melting of densely packed stainless steel powders,* International Journal of Mechanical Sciences, 243, 108034 (2023); https://doi.org/10.1016/j.ijmecsci.2022.108034.

[28] A. Abedini, A. Montazeri, A. Malti, A. Kardani, *Mechanical properties are affected by coalescence mechanisms during sintering of metal powders: Case study of Al-Cu nanoparticles by molecular dynamics simulation,* Powder Technology, 405, 117567 (2022); https://doi.org/10.1016/j.powtec.2022.117567.

[29] J. Nandy, N. Yedla, P. Gupta, H. Sarangi, S. Sahoo, *Sintering of AlSi10Mg particles in direct metal laser sintering process: A molecular dynamics simulation study,* Materials Chemistry and Physics, 236, 121803 (2019); https://doi.org/10.1016/j.matchemphys.2019.121803.

[30] Web source: https://www.lammps.org.

[31] Web source: https://www.ovito.org/.

[32] M. I. Baskes, J. S. Nelson, and A. F. Wright, *Semiempirical modified embedded-atom potentials for silicon and germanium,* Phys. Rev. B, 40(9), 6085 (1989); https://doi.org/10.1103/PhysRevB.40.6085.

[33] B. Jelinek, S. Groh, M. F. Horstemeyer, J. Houze, S. G. Kim, G. J. Wagner, A. Moitra, and M. I. Baskes, *Modified embedded atom method potential for Al, Si, Mg, Cu, and Fe alloys*, Phys. Rev. B, 85(24), 245102 (2012); https://doi.org/10.1103/PhysRevB.85.245102.

[34] A. Malti, A. Kardani, A. Montazeri, *An insight into the temperature-dependent sintering mechanisms of metal nanoparticles through MD-based microstructural analysis*, Powder Technol., 386, 30 (2021); https://doi.org/10.1016/j. powtec.2021.03.037.

[35] W.D. Kingery, M. Berg, *Study of the initial stages of sintering solids by viscous flow, evaporation-condensation, and self-diffusion*, J. Appl. Phys., 26 (10), 1205 (1955); https://doi.org/10.1063/1.1721874.

[36] J. P. Hansen, I. R. McDonald, Theory of Simple Liquids (Fourth Edition) (Elseiver, Amsterdam, 2013); https://doi.org/10.1016/C2010-0-66723-X.

[37] J.C. Slater, Atomic Radii in Crystals, The Journal of Chemical Physics., 41(10), 3199 (1964); https://doi.org/10.1063/1.1725697.

[38]   E. Clementi, D.L.Raimondi, W.P. Reinhardt, *Atomic Screening Constants from SCF Functions. II. Atoms with 37 to 86 Electrons*, The Journal of Chemical Physics., 47(4), 1300 (1967); https://doi.org/10.1063/1.1712084.

[39] Y. Waseda, The Structure of Non-Crystalline Materials: Liquids and Amorphous Solids (McGraw-Hill International Book Company, New York, 1980);

[40] B. E. Douglas, S. -M. Ho, Structure and Chemistry of Crystalline Solids (Springer, New York, 2006); https://doi.org/10.1007/0-387-36687-3.

[41] A. L. Efros and M. Rosen, *The Electronic Structure of Semiconductor Nanocrystals,* Annu. Rev. Mater. Sci., 30, 475 (2000); https://doi.org/10.1146/annurev.matsci.30.1.475.

[42] S.C. Erwin, L. Zu, M.I. Haftel, et al., *Doping semiconductor nanocrystals,* Nature, 436, 91 (2005); https://doi.org/10.1038/nature03832.

[43] G. M. Dalpian and J.R. Chelikowsky, *Self-Purification in Semiconductor Nanocrystals,* Phys. Rev. Lett., 96, 226802 (2006); https://doi.org/10.1103/PhysRevLett.96.226802.

І. Штаблавий, Н. Попільовський, Ю. Никируй, С. Мудрий

Селективне лазерне спікання аморфних наночастинок: моделювання методом молекулярної динаміки

Кафедра фізики металів Львівського національного університету імені Івана Франка, Львів, Україна,
ihor.shtablavyi@lnu.edu.ua

В роботі досліджено процес рідкофазного спікання аморфних наночастинок на основі заліза методом молекулярної динаміки. Для моделювання використано пакет для класичної молекулярної динаміки LAMMPS. Візуальний аналіз атомних конфігурацій наночастинок під час їхнього швидкого охолодження дозволив виявити ефект самоочищення частинок. Для аналізу атомної структури наночастинок після спікання використали парціальні парні кореляційні функції та функції розподілу координаційних чисел. В результаті аналізу основних структурних параметрів, які отримали з використанням вказаних функцій встановили відмінності атомного складу та структури об'єму та поверхні наночастинок.

Ключові слова: Селективне лазерне плавлення, наночастинки, рідкофазне спікання, метод молекулярної динаміки, парні кореляційні функції, функції розподілу координаційних чисел.